Comput Geosci
DOI 10.1007/s10596-009-9130-5

ORIGINAL PAPER

Image analysis algorithms for estimating porous media multiphase flow variables from computed microtomography data: a validation study

Mark L. Porter · Dorthe Wildenschild

Received: 8 August 2008 / Accepted: 13 January 2009

Abstract Image analysis of three-dimensional microtomographic image data has become an integral component of pore scale investigations of multiphase flow through porous media. This study focuses on the validation of image analysis algorithms for identifying phases and estimating porosity, saturation, solid surface area, and interfacial area between fluid phases from gray-scale X-ray microtomographic image data. The data used in this study consisted of (1) a two-phase high precision bead pack from which porosity and solid surface area estimates were obtained and (2) three-phase cylindrical capillary tubes of three different radii, each containing an air–water interface, from which interfacial area was estimated. The image analysis algorithm employed here combines an anisotropic diffusion filter to remove noise from the original gray-scale image data, a k-means cluster analysis to obtain segmented data, and the construction of isosurfaces to estimate solid surface area and interfacial area. Our method was compared with laboratory measurements, as well as estimates obtained from a number of other image analysis algorithms presented in the literature. Porosity estimates for the two-phase bead pack were within 1.5% error of laboratory measurements and agreed well with estimates obtained using an indicator kriging segmentation algorithm. Additionally, our method estimated the solid surface area of the high precision beads within 10% of the laboratory measurements, whereas solid surface area estimates obtained from voxel counting and two-point correlation functions overestimated the surface area by 20–40%. Interfacial area estimates for the air–water menisci contained within the capillary tubes were obtained using our image analysis algorithm, and using other image analysis algorithms, including voxel counting, two-point correlation functions, and the porous media marching cubes. Our image analysis algorithm, and other algorithms based on marching cubes, resulted in errors ranging from 1% to 20% of the analytical interfacial area estimates, whereas voxel counting and two-point correlation functions overestimated the analytical interfacial area by 20–40%. In addition, the sensitivity of the image analysis algorithms on the resolution of the microtomographic image data was investigated, and the results indicated that there was little or no improvement in the comparison with laboratory estimates for the resolutions and conditions tested.

Keywords Multiphase flow · Porous media · Computed microtomography · Image analysis · Marching cubes

1 Introduction

In recent years, significant strides have been made in nondestructive imaging of materials and processes related to the Earth's subsurface. Advances in experimental and analytical techniques have made it possible to characterize and distinguish microscale characteristics such as pore geometry, pore network connectivity, fluid phase distributions in porous media, interfacial

M. L. Porter (✉) · D. Wildenschild
School of Chemical, Biological and Environmental Engineering (CBEE), Oregon State University, Corvallis, OR 97331, USA
e-mail: porterma@engr.orst.edu

D. Wildenschild
e-mail: dorthe@engr.orst.edu

Published online: 06 February 2009

properties, and solute transport variables. Computed microtomographic (CMT) imaging studies have been presented in the fields of: (1) petroleum engineering, focusing on the extraction of pore morphology, network information, and relative permeability estimates for use in pore network simulators (e.g., [4, 13, 28, 33, 36, 39, 40, 49, 53]); (2) environmental engineering where the focus has been on describing nonaqueous phase liquid (NAPL) characteristics such as blob morphology (e.g., [1, 2, 44, 45]) and fluid–fluid-specific interfacial area (e.g., [6, 7, 14–16]); (3) geology and geochemistry [3, 5, 8, 19, 25, 50]; (4) vadose zone and root zone processes (e.g., [11, 12, 22, 43, 54, 55]); (5) and microbiology (e.g., [51]).

Images produced with CMT are gray scale, and therefore need further processing before the properties of interest can be quantified. The gray-scale voxels reflect the large spectrum of X-ray attenuation values of the scanned materials. Generally, segmentation or classification of gray-scale images results in a data set in which each separate entity, hereafter phase, in the image is represented by a single integer value. For example, in a porous material the solids and the void space may be represented by zeros and ones, respectively. Numerous segmentation routines have been presented in the literature (e.g., [32, 34, 35, 38, 48]), and Sezgin and Sankur [47] provide a comprehensive survey of 40 segmentation methods. The segmented data is typically used to quantify properties such as phase distributions (i.e., porosity and saturation). However, the resulting estimates are known to vary significantly depending upon the original image quality and the segmentation method employed [46]. Furthermore, CMT images of porous materials often contain features at or below the image resolution which blur the edges at phase boundaries, which can result in the loss of significant features and errors in the resulting macroscopic estimates [48].

Interfacial area estimates are typically obtained from the segmented data with additional processing. The simplest estimate consists of counting the faces of voxels that exist between two phases; however, this approach results in interfacial area estimates with significant pixelation effects, generally leading to an overestimation for the smooth fluid–fluid interfaces of interest. More advanced approaches include marching cubes methods [17, 30], two-point correlation functions [29, 31] and adaptive distance gradient filtering [18]. McClure et al. [30] recently developed a porous media marching cubes (PMMC) algorithm, which extracts interfacial area estimates directly from gray-scale data, bypassing the need for a segmentation routine.

The primary objectives of this study are (1) to present a detailed description of the image analysis algorithms employed in current and previous investigations by [15, 16, 54], including recent improvements that affect the resulting estimates and (2) to validate these algorithms by comparing phase distribution and interfacial area estimates for a high precision glass bead pack, as well as fluid configurations within capillary tubes, to laboratory measurements and estimates obtained from some of the more commonly used image processing methods and software packages specifically designed for applications to porous media.

2 Image analysis

2.1 Image filtering

Image analysis begins with the reconstructed gray-scale images. Typically, the gray-scale images contain a certain level of noise that can greatly affect the quality of the subsequent segmentation. With this in mind, edge preserving noise reduction filters are commonly used and recommended as a first step in image analysis [23, 48].

Culligan et al. [15, 16] employed a median filter to remove noise from the original gray-scale images. The median filter is a commonly used low-pass, edge preserving nonlinear digital filter that uses the median value of a specified convolution kernel to smooth the data [20] and performs well with outliers (i.e., random noise) [23]. Thus, it considers a neighborhood surrounding the voxel in consideration and replaces that voxel with the median value of the neighborhood. A drawback to the median filter, and other filters based on convolution kernels, is that they blur sharp edged features present in the original image [23]. Thus, our improved image analysis algorithm uses an anisotropic diffusion filter[1] to remove noise from the original gray-scale images. The anisotropic diffusion filter is a mathematically formulated diffusion process that promotes intra-region smoothing over edge smoothing [21, 37]. The equation takes the following form [21]:

$$\frac{\partial u\left(\boldsymbol{x},t\right)}{\partial t} = \nabla\cdot\left(c\left(\boldsymbol{x},t\right)\nabla u\left(\boldsymbol{x},t\right)\right) \tag{1}$$

where the vector $\boldsymbol{x}$ represents the spatial coordinates within the image, t represents the number of times (iterations) the filter is applied to the image, $u\left(\boldsymbol{x},t\right)$ is the voxel intensity, and $c\left(\boldsymbol{x},t\right)$ is a diffusion function that controls the strength of diffusion based on intensity

[1] Daniel Simoes Lopes, http://www.civil.ist.utl.pt/~danlopes

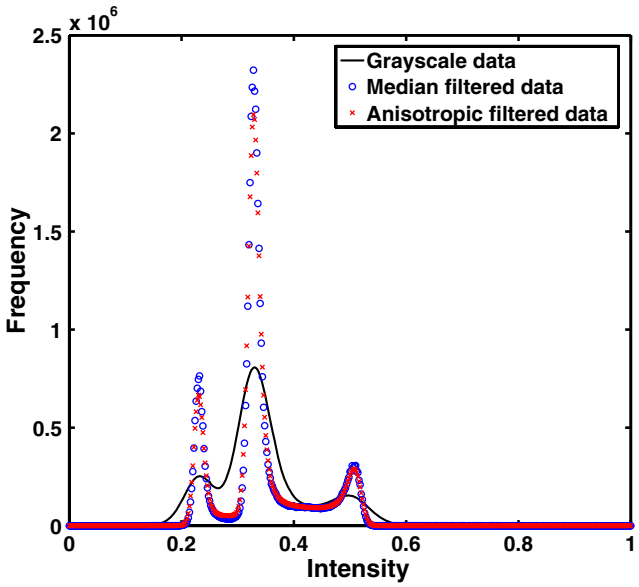

Fig. 1 Comparison of the intensity histograms for the two filters with the original gray-scale data shows that the majority of the smoothing occurs in regions of similar intensities (i.e., there was a reduction of the variance of each peak). The *left*, *middle*, and *right peaks* represents the nonwetting, solid, and wetting phases, respectively

gradients. Perona and Malik [37] and Gerig et al. [21] proposed the following functions for $c(\boldsymbol{x}, t)$:

$$c(\boldsymbol{x}, t) = \exp\left(-\left(\frac{|\nabla u(\boldsymbol{x}, t)|}{\kappa}\right)^2\right) \tag{2}$$

$$c(\boldsymbol{x}, t) = \frac{1}{1 + \left(\frac{|\nabla u(\boldsymbol{x}, t)|}{\kappa}\right)^2} \tag{3}$$

where κ is a parameter chosen according to the level of noise and strength of edges contained in the image. In the discrete case, the anisotropic diffusion filter estimates local gradients as differences between neighboring voxels. If the gradient is large, a discontinuity is assumed and the diffusion process is stopped.

Figure 1 compares the histograms for each filter and an original gray-scale image. It is apparent that both filters reduce the variance in the intensity peaks, thus indicating that the majority of the filtering occurs within regions containing similar intensity values. Additionally, a comparison between the original gray-scale, median-filtered, and anisotropic diffusion-filtered images is provided in Fig. 2. This figure illustrates, qualitatively, that both filters removed a significant amount of noise and preserved edges relatively well. The intensity values for a cross section of the gray-scale, median-filtered, and anisotropic filtered images are also shown in Fig. 2. The intensity values at the phase boundaries provide a measure of the sharpness of the phase boundaries in the original gray-scale images and indicate the degree to which each filter enhances that sharpness. Close inspection of the intensity values for the gray-scale image reveals that the edges between the different phases were originally relatively smooth, and the sharpness of the phase boundaries was not significantly increased using the median or the anisotropic diffusion filter. Multiple κ values were tested using Eqs. 2 and 3 with similar results. Kaestner et al. [23] proposed using a gradient image smoothed by a Gaussian filter for $c(\boldsymbol{x}, t)$ in Eq. 1; however, this was not tested in this study. Applications of the anisotropic diffusion filter (using Eqs. 2 and 3) to CMT data collected at higher resolution, at a different synchrotron source, showed

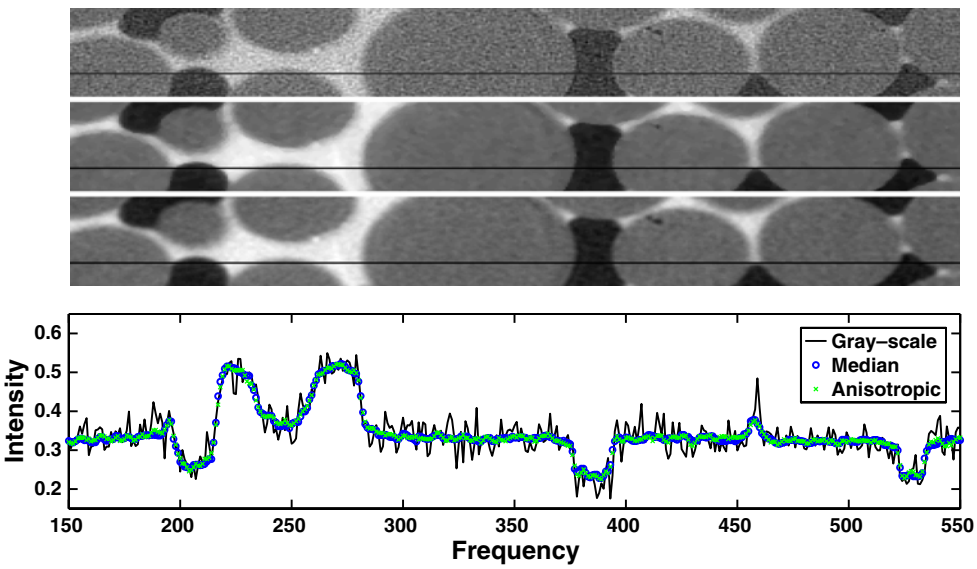

Fig. 2 A comparison between the original gray-scale (*top*), median-filtered (*middle*) and anisotropic diffusion-filtered (*bottom*) images. The graph shows a cross section of the intensity values for each image (*the horizontal line*) indicating that there was very little difference between the median and anisotropic diffusion filter

that phase boundaries were well preserved and the sharpness visibly enhanced with appropriate choices of κ. Thus, the quality of the original gray-scale image had a significant effect on the sharpness of the phase boundaries, which in turn influenced the outcome of the k-means cluster analysis, as will be discussed in the following section.

2.2 Segmentation

In this study, and related works [15, 16, 54], a k-means cluster analysis (included in the CCHIPS software package[2]) was the primary algorithm used to segment both two- and three-phase CMT data. Briefly, the algorithm requires an initial guess for the cluster centers, then iteratively updates the centers until an objective function, namely the squared error function, is optimized. The k-means algorithm has the following drawbacks: (1) there are no spatial constraints, (2) each cluster is characterized by a constant intensity, and (3) obtaining the global optimum is not guaranteed [35], which motivated the comparison with the indicator kriging algorithm (defined later).

In practice, the CCHIPS k-means cluster analysis worked well with two-phase data, but did not properly segment three-phase data sets that did not contain sufficiently sharp intensity gradients between the fluid-fluid interfaces. In the three-phase case, the CCHIPS routine produced segmented data with a thin film of solid phase assigned to all fluid–fluid interfaces indicating that a thin region of intermediate intensity voxels exists between the wetting (high intensity) and nonwetting (low intensity) phases. This likely occurs because the phase boundaries in the original gray-scale images were relatively smooth. To overcome this problem, Wildenschild et al. [54] and Culligan et al. [15, 16] worked the k-means cluster analysis into a larger segmentation algorithm (hereafter, referred to as Autoseg). Briefly, the Autoseg algorithm combined histogram specification, dilation and erosion operations, an edge detection routine (the Canny operator) and a medial axis routine along with the k-means cluster analysis, and most importantly, knowledge of the solid phase locations obtained from a two-phase dry image. Although this algorithm worked for the data presented in Wildenschild et al. [54] and Culligan et al. [15, 16], applications to recent CMT data resulted in the faulty creation of wetting phase regions around some of the solids, features that were not present in the gray-scale image. Additionally, this algorithm was rather complex and computationally intensive, taking approximately 3–4 h per volume (a typical volume was 650×650×515 voxels) on a personal computer. The results obtained using Autoseg are included for comparison purposes only.

The segmentation algorithm used in this study involved only a k-means cluster analysis and knowledge of the solid phase locations from a dry image. The first step in the algorithm consisted of segmenting both wet and dry data sets into binary images using the k-means cluster analysis. For the case of the wet data, the segmentation step created a binary image in which the nonwetting phase was separated from both the wetting and solid phases. The solid and wetting phases were subsequently separated by overlaying the solid phase, obtained from the segmented dry data, onto the segmented (binary) wet data. A post processing step was implemented to remove blobs under a certain size. This was especially useful for removing small artifacts within the beads and small unphysical fluid blobs that were created due to inaccuracies in the segmentation routine and slight movement of the solid phase during the experiments. Figure 3 shows an example of the resulting segmented data from this routine. Qualitatively, the segmented data represents the original data well. Additionally, this algorithm segments a typical data set in approximately 10 min.

In recent applications of the k-means cluster analysis to three-phase data collected at the Advanced Light Source (ALS) beam-line (Lawrence Berkeley National Laboratory), the algorithm properly segmented the data without the need of overlaying the solid data onto the wet data. This is the simplest and most accurate of the three segmentation routines discussed here, since it reduces any error associated with movement of the solid phase. The success of the algorithm when applied

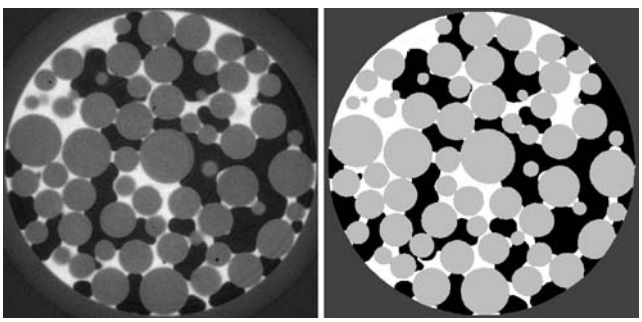

Fig. 3 A comparison of filtered (anisotropic diffusion) gray-scale image (*left*) with k-means segmented image (*right*). The *white*, *black*, and *light gray region*s are water, NAPL, and solids, respectively

[2]Copyright 2001, The Imaging Research Center, Children's Hospital Medical Center, Cincinnati, OH, USA http://www.irc.cchmc.org/cchips.php

to the ALS data set is most likely due to the fact that the phase edges in the original gray-scale images were sharper than those obtained from Advanced Photon Source (APS) beam-line (Argonne National Laboratory), likely because of a better signal-to-noise ratio during data collection. This led to edge enhancement during the filtering step (see Section 2.1) and, thus the k-means algorithm easily identified the nonwetting–wetting phase interface.

Porosity and saturation values were estimated from the segmented data via voxel counting. This is the simplest and most widely used method for these types of estimates. Two-point correlation functions may also be used for these estimates; however, Lindquist et al. [29] showed that there was little difference in the estimates obtained with either method.

2.3 Interfacial area

Compared to the number of segmentation methods, relatively few algorithms have been presented in the literature for estimating interfacial area from CMT image data. Some of these include voxel counting, marching cubes (MC), two-point correlation functions, and adaptive distance gradient filtering (ADGF). Counting voxel faces common to the two phases of interest is by far the simplest method; however, in cases pertaining to fluid–fluid interfaces in porous media where the surfaces are smooth, the estimates are high. Lindquist et al. [29] stated that voxel counting estimates should be considered as upper bounds for interfacial area.

MC algorithms have recently been employed in a number of porous media studies [15–17, 30, 31] and one advantage of this method is that it can be applied directly to the gray-scale data [30]. The MC algorithm constructs an isosurface composed of a triangular mesh that correspond to a chosen isovalue (or threshold). Thus, the isovalue and the information from the surrounding voxels determines the isosurface. For example, in a binary image where each phase is represented by a one or a zero, an optimal choice of the isovalue is 0.5 since the resulting isosurface is halfway between two adjacent voxels of different phases. Dalla et al. [17] used synthetic binary data to investigate the accuracy of the marching cubes algorithm for wetting phase bridges encountered in porous media and showed that the estimated area was generally lower than an analytical estimate.

Other methods for estimating interfacial area from CMT image data include two-point correlation functions and ADGF. Lindquist et al. [29] and Song et al. [50] compared interfacial area estimates obtained from two-point correlation functions and voxel counting. Their results showed that voxel counting resulted in estimates that were 1.5–2.9 times higher than estimates obtained from two-point correlation functions. Montemagno and Ma [31] compared two-point correlation functions and marching cubes interfacial area estimates for binary data of synthetic sphere packings and single spheres, and showed that the two-point correlation functions obtained smaller relative errors than MC and that MC is sensitive to pixelation effects. Flin et al. [18] compared their ADGF algorithm to MC applied to binary and smoothed binary data, and for measured surface area estimates of three snow samples observed relatively similar results from all methods, except for MC applied to Gaussian smoothed binary data, which they claim was a result of the large ($11\times11\times11$) kernel used in the Gaussian filter.

Interfacial area estimates presented here, and in related works (see [15, 16]), were obtained using the commercially available image analysis software, Amira™, which uses a generalized marching cubes algorithm to generate an isosurface between phases. The isosurfaces are generated by choosing a single isovalue that effectively separates one phase from all other phases in the image. Isosurfaces are generated for the total interfacial area for the solid phase, a_s, wetting phase, a_w, and nonwetting phase a_n. In a three-phase system, the total interfacial area for each phase is defined as follows:

$$\begin{aligned} a_s &= a_{ws} + a_{ns} \\ a_w &= a_{nw} + a_{ws} \\ a_n &= a_{nw} + a_{ns} \end{aligned} \tag{4}$$

where a_{nw} is the interfacial area of the nonwetting–wetting interface, a_{ns} is the interfacial area of the nonwetting–solid interface, and a_{ws} is the interfacial area of the wetting–solid interface. From Eq. 4, it can be shown that the interfacial area between two phases is defined as follows:

$$\begin{aligned} a_{nw} &= \frac{1}{2}\left(a_w + a_n - a_s\right) \\ a_{ns} &= \frac{1}{2}\left(a_n + a_s - a_w\right) \\ a_{ws} &= \frac{1}{2}\left(a_w + a_s - a_n\right). \end{aligned} \tag{5}$$

In many studies concerning interfacial area in porous media, a_{nw} is of interest [6, 9, 10, 15, 16] and the use of Eq. 5 is common. It should be noted that Eq. 5 will propagate any error associated with the estimates of a_w, a_n and a_s when these are the measured values. This

is especially important when using the marching cubes algorithm to estimate a_w, a_n, and a_s, since it is often difficult to obtain perfect contact between the three isosurfaces. For example, consider a trinary data set in which the nonwetting, solid, and wetting phases are assigned the values 0, 1, and 2, respectively; one would need multiple isovalues and a second binary data set for one of the phases to construct satisfactory isosurfaces of a_w, a_n and a_s. Culligan et al. [15, 16] used a method that involved a trinary data set for estimating a_n and a_w and a separate binary data set for a_s. In their case, the trinary values were 3, 5, and 10 for the nonwetting, solid, and wetting phases, respectively. The isovalues selected were 4 and 7.5 for a_n and a_w, respectively. For the binary data set, the values for the nonwetting phase and solid phase were 0 and 1, respectively, and an isovalue of 0.5 was selected. Additionally, the data were resampled in Amira™ prior to applying MC. The resampling step smoothed the data and coarsened the grid using a triangle window. The grid coarsening was necessary at the time because of computational memory constraints (2 GB). Although it was determined that this method resulted in good surface area estimates for a binary sphere [15], a number of issues arise with this method when applied to three-phase porous media data. The first issue involves the use of a single isovalue in a trinary data set to estimate a_w or a_n. Using an isovalue of 4 for a_n resulted in an isosurface that was biased toward the nonwetting phase at all nonwetting–wetting interfaces. In a similar fashion, the use of an isovalue equal to 7.5 for a_w resulted in an isosurface biased toward the wetting phase at all nonwetting–wetting interfaces. This ultimately resulted in isosurfaces that had little or no contact at all nonwetting–wetting interfaces, thus introducing some error in approximations based on Eq. 5 (however, as shown later, the errors were still less than 20% when compared to estimates based on laboratory measurements).

Our improved interfacial area estimation method converts the segmented trinary data into three (one for each phase) different binary data sets in which each phase is separated from the other two phases. For example, in the nonwetting data set, the nonwetting phase is set equal to zero and both the wetting and solid phases are set equal to one. This allows for the use of a single isovalue for the construction of all isosurfaces. An isovalue equal to 0.5 was chosen for a_w, a_n and a_s, which ensures maximal contact between the isosurfaces. This is similar to the approach Dalla et al. [17] applied to synthetic binary data. Additionally, we smooth the binary data with a Gaussian filter (3×3×3 kernel) to reduce pixelation effects in the resulting isosurfaces.

McClure et al. [30] recently proposed a mathematically rigorous porous media marching cubes (PMMC) algorithm, which we compare our method to in this study. PMMC was developed to address many of the issues that arise when applying the marching cubes algorithm to segmented data. Additionally, this algorithm estimates other properties including interfacial curvature and three-phase contact lines; however, only a few key aspects pertaining to interfacial area estimates are discussed here (for further details see [30]). PMMC uses the standard generalized marching cubes algorithm for the fluid and solid phases except when a nonwetting–wetting–solid contact line is encountered. It is precisely in these locations that Dalla et al. [17] observed that the standard marching cubes algorithm did not faithfully represent the wetting phase surface. In these cases, PMMC employs a combination of the marching cubes, interpolation, and extrapolation to accurately construct the isosurface. Furthermore, PMMC estimates the interface of interest, (i.e. a_{nw}, a_{ws}, a_n, etc...) directly, bypassing the need for Eq. 5. Since PMMC can directly estimate the interface of interest, it is possible to use the original gray-scale data, thus avoiding the segmentation step. It is noted that the interfacial area estimates are affected by the original noise in the data and McClure et al. [30] recommends the use of a smoothing filter.

3 Validation methods

3.1 Experimental data sets

The experimental data presented here was collected at the GeoSoilEnviro Consortium for Advanced Radiation Sources beam-line at the APS, Argonne National Laboratory. Only the most necessary details pertaining to the APS beam-line specifications will be presented here, further details can be found in Wildenschild et al. [54, 55]. The experiments were conducted at an energy level just above the K-shell photoelectric absorption edge of iodine (33.2 keV). An 11% (by weight) iodine-spiked water solution was used as the wetting phase in these experiments to facilitate X-ray absorption in the wetting phase, resulting in an intensity distribution from which the nonwetting and wetting phases could be distinguished. A tunable monochromator isolates a single energy, 33.27 keV, from the white synchrotron light and the X-rays pass through the sample and are subsequently converted to visible light by a scintillator and captured on a high-speed CCD camera. The raw data is processed with a series of algorithms developed in IDL™ (Research Systems Inc.) that sharpen

edges, remove ring artifacts, center the data, and then reconstruct the gray-scale images via a filtered back-projection algorithm [41].

The experimental data consisted of CMT images of (1) a high precision bead pack and (2) cylindrical capillary tubes of three different radii, each containing an air–water interface. The high precision beads ($d = 0.8 \pm 0.01$ mm, $\rho = 2.5$ g cm^{-3}, per manufacturer specifications, Glenn Mills Inc.) were packed into an acrylic column (i.d. = 6.54 mm). The beads were assumed to be clean since the manufacturer polished and washed them prior to packaging. The mass of the beads packed in the column was 233.0 ± 0.5 mg. Based on this information, the number of beads in the column and the surface area for the entire bead pack was estimated to be 348 ± 8 beads and $700 \pm 20\,\text{mm}^2$, respectively. The bead pack was imaged at two different resolutions, namely 11.8 and 5.9 μm. The two different resolutions were obtained by adjusting the region of interest (ROI) using a binning procedure. The higher resolution (5.9 μm) data was imaged with a Micromax CCD camera equipped with a Nikon macro lens and a 10-mm spacer, and the full camera chip (1,300×1,050 voxels) was used. The lower resolution (11.8 μm) data was obtained by binning the voxels 2 by 2 such that a ROI of 650×525 voxels was produced.

Cylindrical capillary tubes with three different radii were used to image three different air–water menisci near equilibrium conditions. The capillary tube dimensions and CMT image resolutions are listed in Table 1. The tubes were secured in a vertical position and the lower end was submerged in a water reservoir while imaging. Cylindrical capillary tubes were chosen so that interfacial area estimates could be compared with interfacial area calculations based on the radius of curvature from Laplace's Law:

$$P_c = P_n - P_w = \frac{2\sigma \cos\theta}{r_t} \tag{6}$$

where σ is the surface tension between air and water, θ is the contact angle and r_t is the radius of the capillary tube. We assumed that the shape of the meniscus could be approximated by a spherical cap, thus $a_{nw} = 2\pi r_c h$, where r_c is the radius of curvature of the meniscus and h is the height of the cap, see Fig. 4. The radius of the tube and the radius of curvature of the meniscus are related by $r_t = r_c \cos\theta$. Values for r_c and h were obtained independently by two different methods to ensure the resulting estimates were reliable. In the first method, r_c and h were measured directly from cross sections (on the principle x- and y-axes) of the gray-scale images. In the second method, the contact angle between the meniscus and the capillary tube was measured along the principle x- and y-axes of gray-scale images, and values for r_c and h were then calculated based on θ and the radius of the tubes, r_t, using $r_t = r_c \cos\theta$ and $r_c = (h^2 + r_t^2)/2h$. The values obtained from the measurements and calculations are listed in Table 2, which shows that there was little difference between the measured and calculated values for r_c. However, there were noticeable differences between the measured and calculated h values. Based on these observations, the calculated values of r_c and h (columns 5 and 6, respectively) in Table 2 were used to calculate analytical estimates of a_{nw} for the air–water menisci. It is noted that the estimated contact angle of 22° for the 1,350-μm tube is higher than expected. One possible explanation for this high value is that the meniscus had not reached equilibrium. Despite the high contact angle the resulting calculated value of r_c is consistent with the corresponding measured value.

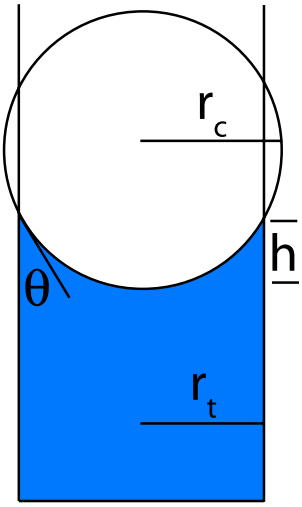

Fig. 4 Illustration of a cross section of the air–water meniscus in a capillary tube where r_t is the radius of the tube, r_c is the radius of curvature of the meniscus, θ is the contact angle, and h is the height of the spherical cap

Table 1 List of capillary tube inside diameters and the associated CMT image resolutions

Inside diameter (μm)	CMT image resolution (μm)
800 ± 8	13, 6.5
$1{,}350 \pm 25.4$	13
$1{,}500 \pm 15$	13, 6.5, 3.3, 1.6

3.2 Image processing methods

The majority of CMT data reported in the literature is subjected to image analysis techniques similar to those discussed in Section 2 prior to the estimation of porosity, saturation, and interfacial area; thus, it is important to note that the potential for error is relatively high. However, there is no straightforward way to assess the error associated with the estimates

Table 2 Measured and calculated values for predicting the interfacial area of the meniscus in the capillary tubes assuming the meniscus was the shape of a spherical cap (i.e., $a_{nw} = 2\pi r_c h$)

Tube	Measured			Calculated	
i.d. (μm)	r_c (mm)	h (mm)	θ (deg)	r_c (mm)	h (mm)
800	0.40	0.36	6	0.40	0.36
1,350	0.73	0.44	22	0.73	0.46
1,500	0.76	0.66	3	0.75	0.71

since they are affected by (1) the noise in the original image, (2) smoothing of edges when filtering the noise, (3) improper segmentation of some voxels near phase boundaries, (4) the sensitivity of MC to pixelation effects, and (5) the possibility of poor contact between isosurfaces.

In order to assess the reliability and validate the image analysis method presented here, we have calculated porosity and interfacial area estimates for the experimental systems described in Section 3.1. First we estimated the porosity of the two-phase high precision beads using our k-means segmentation routine and an indicator kriging algorithm; then compared the results with estimates based on laboratory measurements. Indicator kriging was conducted using 3DMA[3] and is described in full detail by Oh and Lindquist [32]. Briefly, indicator kriging is a local thresholding method that incorporates spatial information through the spatial two-point covariance of the image [32]. The method requires a population assignment step, which segments a fraction of the image based on two threshold values T_0 and T_1. Care must be taken in the choice of T_0 and T_1 since misclassification can occur. Oh and Lindquist [32] developed automated methods for selecting T_0 and T_1; however, based on their experience, they recommend user selection [27]. Indicator kriging was chosen for comparison with k-means cluster analysis because it accounts for spatial correlations within the image, whereas k-means does not. Furthermore, 3DMA is a software package specifically designed for applications in porous media, and therefore allows for comparison of our approach to another commonly used algorithm.

Numerous interfacial area estimates for the high precision glass beads and menisci in the capillary tubes were calculated using various combinations of the image analysis techniques discussed in Section 2 and are described in detail here. Table 3 lists the various interfacial area estimation methods and the image analysis techniques used to obtain each estimate. The first column lists the names we have used to identify the different interfacial area estimates. The 2-point correlation estimates were obtained using the method described by Torquato [52, pg. 290] and the algorithm was implemented as described in [42]. The method entitled Gauss MC is the method we have used in recent studies and is a replacement for the Culligan method, which was used in [15, 16]. Blob3D[4] refers to estimates obtained using the freely available image analysis software package developed by Ketcham [24]. Blob3D uses a MC algorithm to construct isosurfaces from which interfacial area estimates are obtained. In practice, we found that Blob3D created surfaces on the flat edges of the square volumes that contained the capillary tube data; thus, we were not able to obtain reliable interfacial area estimates from Blob3D for the capillary tube data. This artifact was not an issue with the high precision beads since the beads were not in contact with the edges of the volume. The "Filter" column lists the filter used to remove noise from the original gray-scale data and, in parentheses, indicates the number of times (or iterations) the filter was applied to the data. The "Segmentation" column indicates which segmentation method was used to classify the phases. For the high precision glass beads, both k-means and indicator kriging segmentation routines were used in order to investigate the effect of the segmentation routine on the resulting surface area and interfacial area estimates. In the case of PMMC, no segmentation routine was required. The last column, entitled "Data type," indicates the type of data from which the estimate was obtained and in most cases binary data from the listed segmentation routine were used to obtain interfacial area estimates. In the Median MC and Gauss MC, the respective filter kernels were 3×3×3 so that the edges of each phase were the only areas affected by the filter. The median filter was chosen since (in a binary image) it does not smooth the data, it only rearranges the binary values near edges based on the surrounding neighbors.

[3] http://www.ams.sunysb.edu/~lindquis/3dma/3dma_rock/3dma_rock.html

[4] http://www.ctlab.geo.utexas.edu/software/index.php

Table 3 List of the different methods used to obtain interfacial area and surface area estimates and the corresponding image analysis steps

Method	Filter	Segmentation	Data type
Voxel counting	Anisotropic diffusion (×1)	k-means and indicator kriging	Binary
2-point correlation	Anisotropic diffusion (×1)	k-means and indicator kriging	Binary
Binary MC	Anisotropic diffusion (×1)	k-means and indicator kriging	Binary
Median MC	Anisotropic diffusion (×1)	k-means and indicator kriging	Median-filtered binary
Gauss MC	Anisotropic diffusion (×1)	k-means and indicator kriging	Gauss-filtered binary
Resample MC	Anisotropic diffusion (×1)	k-means and indicator kriging	Resampled trinary
Blob3D	Anisotropic diffusion (×1)	k-means and indicator kriging	Binary
PMMC	Median (×2)	–	Gray scale
Culligan method	Median (×1)	Autoseg	Resampled trinary

This effectively tests the sensitivity of interfacial area estimates to the segmentation routine. The Gaussian filter, on the other hand, smoothed the binary data. A smoothing filter was chosen since it has been shown that the marching cubes algorithm is sensitive to pixelation effects [17, 30, 31], although to a lesser extent than voxel counting. In both the Median MC and Gauss MC, an isovalue of 0.5 was selected and good contact between each isosurface was maintained. In the case of Gauss MC, the smoothing caused some deterioration of contact near the three-phase contact line.

4 Results

4.1 High precision beads (two-phase analysis)

Figure 5 compares the two-dimensional void ratio estimates for each slice obtained from the k-means and indicator kriging segmentation methods for the two resolutions. These results indicate that the two segmentation methods produce virtually the same void ratio estimates and that doubling the resolution had little effect on the estimates. Table 4 compares the volume averaged porosity estimates obtained from laboratory measurements with estimates obtained from the segmented CMT data. These values are reported to three significant figures for comparison purposes only. These results show that all of the estimates were essentially the same with a maximum of 1.5% error, and that the estimates were not notably sensitive to the choice of segmentation routine, nor the different resolutions.

The surface area of the two-phase bead pack was estimated using voxel counting, 2-point correlation functions, Binary MC, Median MC, Gauss MC, Resample MC, and Blob3D (see Table 3) at the 11.8- and 5.9-μm/voxel resolutions. The relative errors (with respect to the laboratory measurement) for all estimates

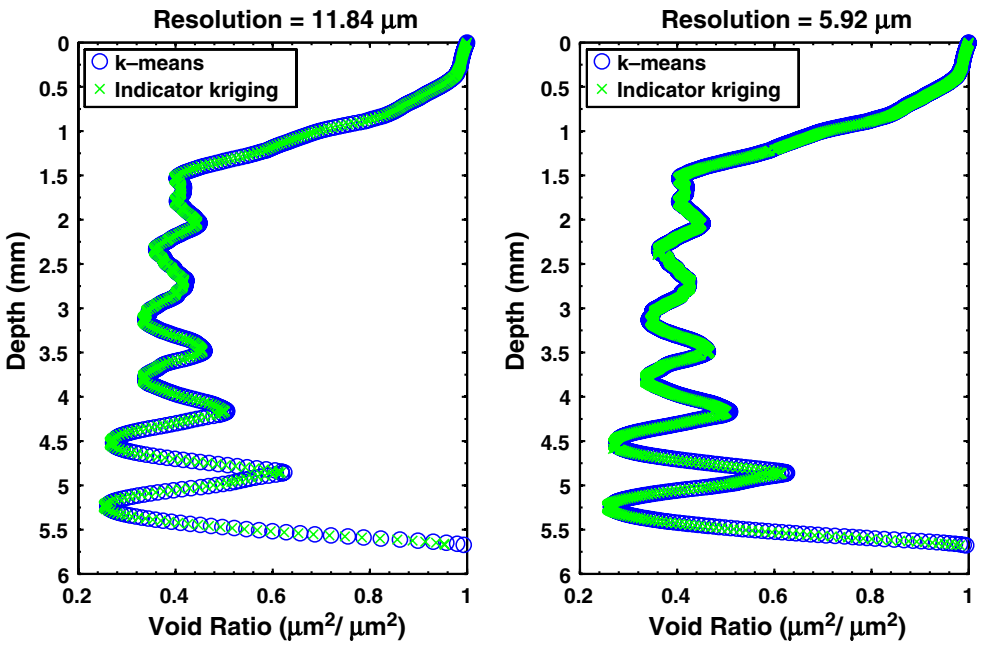

Fig. 5 A comparison of glass bead two-dimensional, void ratio estimates (per slice) as a function depth for k-means and indicator kriging for the low (*left*) and high (*right*) resolution images

Table 4 Comparison of volume averaged porosity estimates obtained from measurements and segmented CMT data

Resolution (μm)	Measured	k-means	Indicator kriging
11.84	0.509	0.515 (1.2% error)	0.510 (0.3% error)
5.92	0.509	0.517 (1.5% error)	0.515 (1.1% error)

are presented in Figs. 6 and 7. The two horizontal lines represent the error associated with the laboratory measurement. Voxel counting and 2-point correlation functions overestimated the interfacial area by more than 25% for the 11.8-μm/voxel and more than 35% for the 5.9-μm/voxel. All other estimates were within 15% and 10% of the laboratory measurement for the 11.8- and 5.9-μm/voxel resolutions, respectively. The Blob3D interfacial area estimates are based on isosurfaces; thus, it is not surprising that they are similar to the other MC methods; however, the Blob3D estimates were higher than all other MC methods. The error associated with the 2-point correlation functions contradicts the results reported by Montemagno and Ma [31]; however, they calculated a_s using the angular average, which appears to be a more accurate method than the one we used here (see [52, pg. 290]). Figures 6 and 7 also show that the estimates were not significantly affected by the segmentation routine; at both resolutions, estimates from indicator kriging were slightly lower than the estimates obtained by k-means cluster analysis. In all cases, the surface area estimates increased slightly, between a factor of 1.04–1.09, as a result of doubling the resolution. Most of the MC methods underestimated the laboratory measurement at 11.8 μm/voxel, whereas at 5.9 μm/voxel the surface area estimates increased slightly and therefore match the analytical estimates more closely for the 5.9-μm/voxel resolution. The observed increase in surface area estimates at the 5.9-μm resolution could be caused by a number of factors. One such factor is the regions near the bead contact points. In the 5.9-μm resolution images, these regions are better resolved than in the 11.8-μm images. In both cases, the images show contact that is greater than the experimental system; however, in the 5.9-μm resolution images, the contact is less, thus potentially contributing to an increase in the surface area estimates.

Doubling the resolution was a relatively easy process at the APS beam-line; however, the decision to do so should not be made lightly since the size of the data increased by a factor of 8. This is especially important if multiple data sets are collected throughout an experiment. The number of voxels in the 11.8- and 5.9-μm/voxel resolution data sets was 650×650×515 (415 MB) and 1,300×1,300×1,030 (3.3 GB), respectively. Thus, the computational demands to store and process the higher resolution data increased signifi-

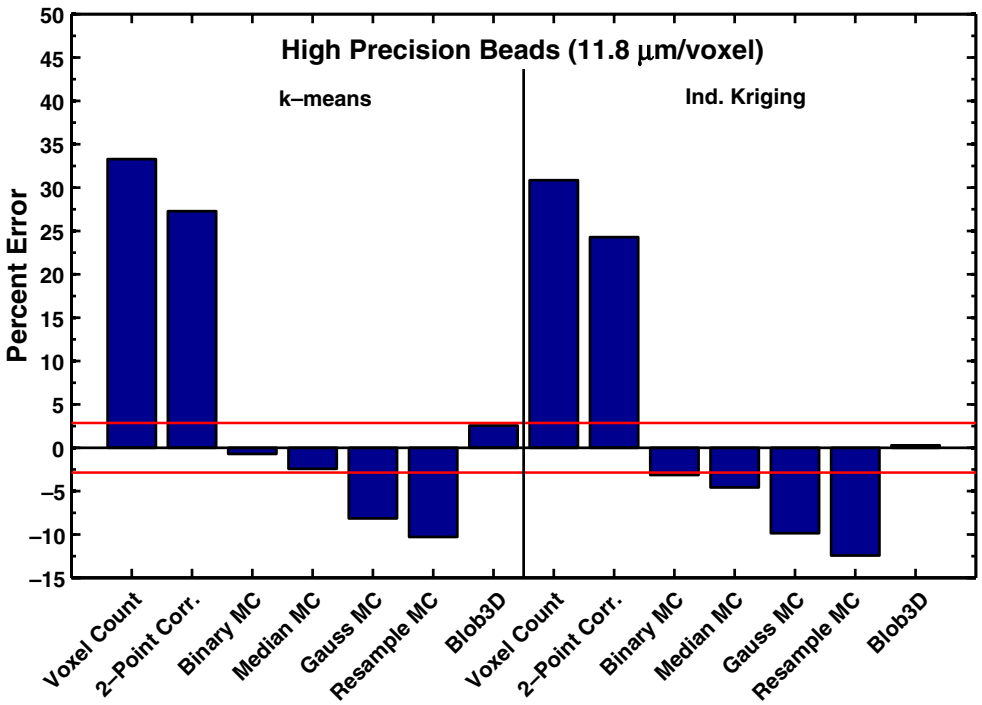

Fig. 6 The relative error obtained from various interfacial area estimation methods for the two-phase, high precision glass beads at a resolution of 11.8 μm/voxel. The figure shows results for k-means and indicator kriging on the left and right, respectively, of the *vertical line*. The *horizontal red lines* represent the error associated with the laboratory measurement

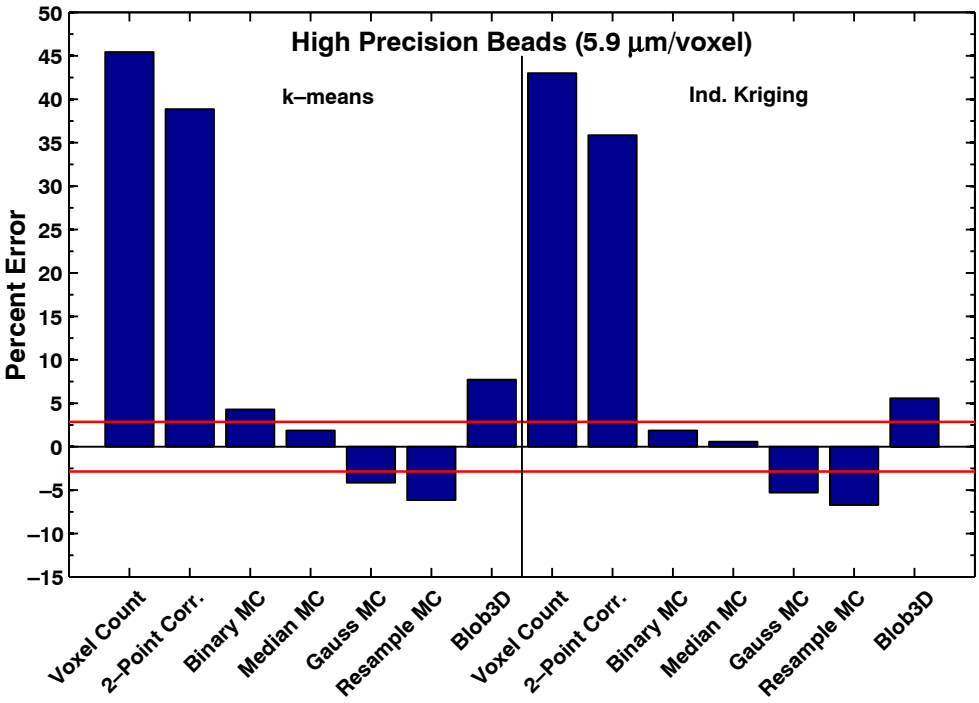

Fig. 7 The relative error obtained from various interfacial area estimation methods for the two-phase, high precision glass beads at a resolution of 5.9 µm/voxel. The figure shows results for k-means and indicator kriging on the *left* and *right*, respectively, of the *vertical line*. The *horizontal red lines* represent the error associated with the laboratory measurement

cantly. The performance of all software used in this study greatly decreased (took longer) when working with the high resolution data. Considering the relatively small differences in the estimates presented here and the significant increase in computational costs, it is questionable if any new insights were gained regarding the porosity and surface area by doubling the resolution.

Although the porosity and surface area estimates presented in this study were not highly sensitive to the segmentation routines used, it is possible that other properties of the porous media (e.g., pore connectivity, permeability, etc.) could be affected by the choice of the segmentation routine and the resolution of the data. This particularly needs to be considered when the regions near bead-to-bead contacts are of importance.

4.2 Capillary tubes (three-phase analysis)

Capillary tube CMT data were collected to test the image analysis methods on a simple three-phase system. The 13-µm resolution data were used to investigate a_{nw} estimates of the air–water interface obtained by voxel counting, 2-point correlation functions, Resample MC, Binary MC, Median MC, Gauss MC, PMMC, and the Culligan method (see Table 3). The values reported for PMMC were provided by James McClure [30]. Voxel counting a_{nw} estimates did not require the use of Eq. 5 since the voxel faces between the phases of interest were counted. 2-point correlation estimates of a_n, a_s, and a_w were obtained as described by Torquato [52, pg. 290] and a_{nw} values were calculated using Eq. 5. All other estimates were obtained using Amira™ and Eq. 5

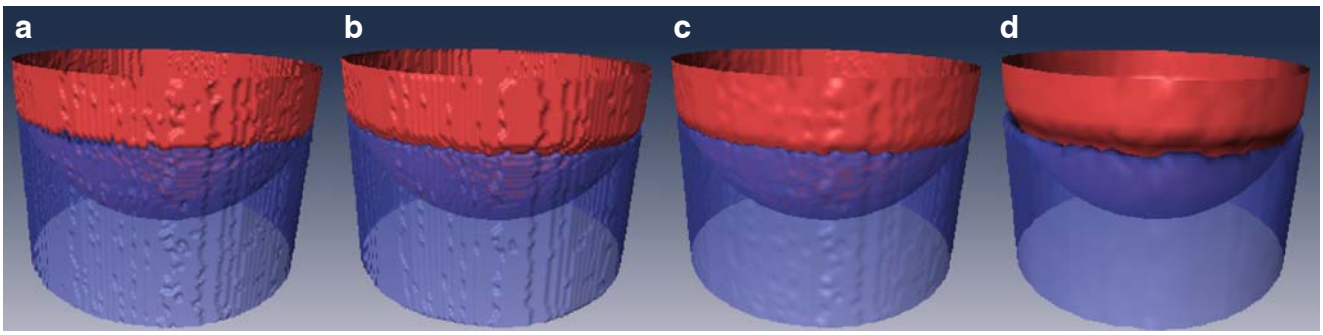

Fig. 8 Comparison of **a** Binary MC, **b** Median MC, **c** Gauss MC, and **d** Resample MC nonwetting (*red*) and wetting (*blue*) phase isosurfaces

Table 5 Comparison of a_{nw} estimates for the air–water meniscus of the 13-μm resolution capillary tubes

	Tube i.d. (μm)		
	800	1,350	1,500
Analytical estimate	0.91	2.08	3.36
Voxel counting	1.23	2.90	4.37
2-point correlation	–	2.57	4.18
Binary MC	0.85	1.99	3.33
Median MC	0.80	1.94	3.15
Gauss MC	0.76	1.84	2.98
Resample	0.76	1.82	2.71
PMMC	0.78	1.93	2.95
Culligan method	0.96	2.30	2.77

All estimates are in units of mm^2

as described in Section 2.3. Estimates from Blob3D were not included here since estimates for a_s, a_n, and a_w obtained with this program included regions associated with the flat edges of the square volume. This was not an issue with the two-phase bead data since none of the solid phase touched the edges. The extra area associated with the edges of the square volume could be subtracted out since those areas are flat surfaces; however, since Blob3D uses isosurfaces to estimate interfacial area, it is expected that the results would be similar to those obtained using Amira™.

The resulting isosurfaces for a_n and a_w produced using Amira™ are provided in Fig. 8. As expected, Binary and Median MC show significant pixelation effects (stair-step appearance), and Binary MC more accurately represented the wetting phase at the three-phase contact line than the Median MC. Gauss MC shows slight signs of pixelation effects, yet was relatively smooth at the three-phase contact line. Resample MC resulted in the smoothest isosurfaces; however, there was no contact at the air–water interface.

The a_{nw} estimates for the air–water interface are listed in Table 5 and the percent error between the analytical a_{nw} estimate and the image analysis estimates for the three capillary tubes (13 μm/voxel resolution) is shown in Fig. 9. The horizontal lines represent the error associated with the analytical estimates. All MC methods underestimated the analytical estimate by 1–20% error, whereas voxel counting and two-point correlation functions overestimated the analytical value by 20–40%. Of all MC methods, the Resample MC method consistently resulted in the greatest percent error, whereas the Binary MC method consistently resulted in the least percent error. This suggests that in the Binary MC method, pixelation effects make up for areas in which the MC method does not accurately capture the geometry of the phase boundary. Estimates

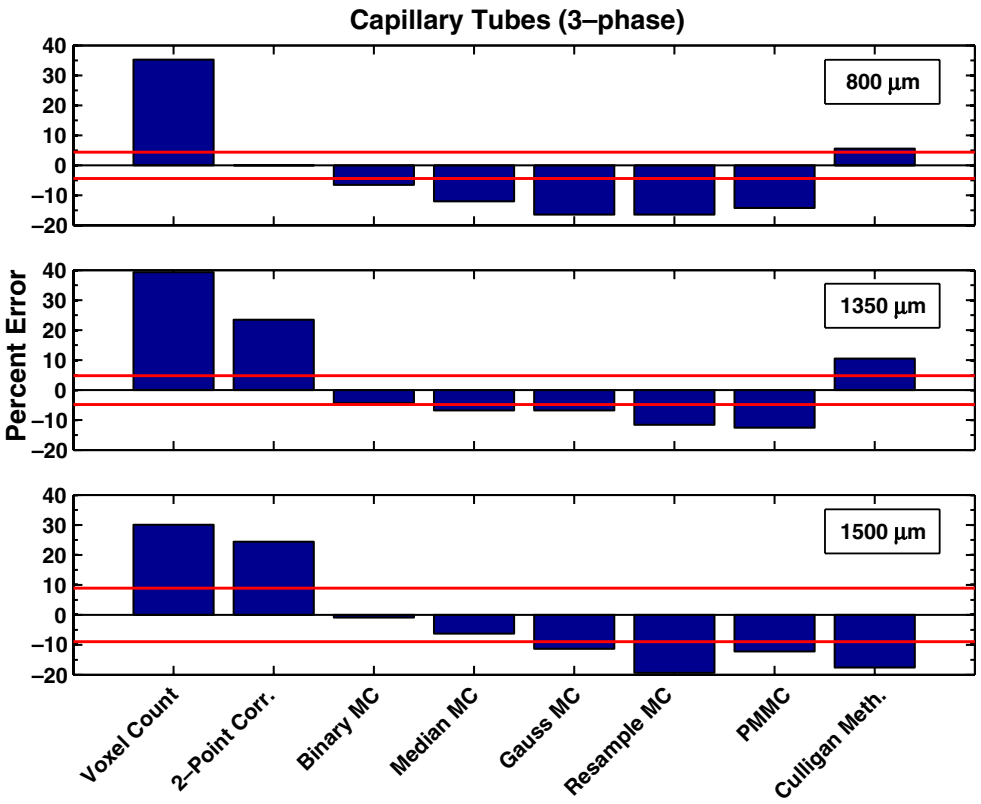

Fig. 9 Relative errors for the a_{nw} estimates obtained from different image analysis techniques for the 13-μm/voxel resolution capillary tube data. The *horizontal red lines* represent the error associated with the analytical estimate

obtained from the Culligan method were the only estimates that were not consistent for all three capillary tubes. Although all estimates from the Culligan method were within 20% error, this method slightly overestimated the analytical estimate for the 800- and 1,350-μm tubes, but underestimated it for the 1,500-μm tube. Since the only difference between resample MC and the Culligan method was the segmentation routine, the results suggest that the segmentation routine (Autoseg) used in Culligan et al. [15, 16] was not as consistent as the segmentation routine (k-means) presented here. In general, all estimates obtained from the MC methods, including the Culligan method, are excellent considering the error associated with the analytical estimate.

The effect of voxel resolution on the resulting a_{nw} estimates was also investigated using the 800- and 1,500-μm capillary tubes. The analysis of the higher resolution CMT data was identical to the analysis of the 13-μm data. The a_{nw} estimates obtained from the high resolution CMT image data are shown in Table 6 along with the 13-μm data. The results show that in both the 800- and 1,500-μm tubes, doubling the resolution caused a decrease in the interfacial area estimates and therefore a decrease in the accuracy of the estimate. This is contrary to what would be expected since there are more voxels available for the construction of the isosurface in the 6.5-μm data than in the 13-μm data. Additionally, at higher resolutions it is expected that features such as the nonwetting–wetting–solid contact line would be better resolved, leading to more representative isosurfaces and a more accurate interfacial area estimate. However, the signal-to-noise ratio does deteriorate as the resolution is increased. Even at a resolution of 3.3 μm (approximately 4 times greater than 13 μm), no significant change in a_{nw} was observed.

Table 6 a_{nw} estimates for a series of voxel resolutions for the 800- and 1,500-μm diameter capillary tubes

Voxel resolution (μm)	Method	800 μm	1,500 μm
	Analytical estimate	0.91	3.36
13	Binary MC	0.85	3.32
	Median MC	0.8	3.15
	Gauss MC	0.76	2.97
6.5	Binary MC	0.83	3.21
	Median MC	0.76	3.10
	Gauss MC	0.75	2.92
3.3	Binary MC	–	3.34
	Median MC	–	3.14
	Gauss MC	–	2.96
1.6	Binary MC	–	5.92
	Median MC	–	5.22
	Gauss MC	–	3.73

Units are in mm^2

This shows that in these capillary tube systems an increase in resolution did not result in an increase in accuracy for the interfacial area estimates. Only at a resolution of 1.6 μm was there considerable increases in the a_{nw} estimates, however the interfacial area was greatly overestimated. The high values in the 1.6-μm data were caused by the significantly increased signal-to-noise ratio encountered in the original gray-scale data for this resolution. To improve signal-to-noise ratios, one can use longer exposure times during data collection; however, the results presented here did not warrant this. It is also possible that minor changes in the image analysis routine (i.e., more iterations of the anisotropic diffusion filter) could have eliminated some of this noise; however, this was not attempted since the goal of this study was to test the image analysis method presented here.

5 Summary and conclusions

In this study, a much needed validation was carried out to test the current techniques and those used in Culligan et al. [15, 16] for analyzing CMT image data to obtain phase distribution and interfacial area estimates. Our technique involved three steps: (1) filtering of the original gray-scale image data with a median or anisotropic diffusion filter, (2) segmentation of the data into binary (or trinary) data sets using a k-means cluster analysis, and (3) construction of isosurfaces from the segmented data using the commercially available software package Amira™, which uses a generalized marching cubes algorithm. Phase distribution estimates such as porosity and saturation were obtained from the segmented data by counting voxels. Interfacial area estimates were obtained from the isosurfaces.

To test the reliability of the image analysis method presented here, two experimental data sets were analyzed and the results were compared to laboratory measurements, as well as results obtained by other image analysis methods currently in use. The two data sets consisted of (1) a high precision bead pack and (2) air–water interfaces contained within three capillary tubes of different radii. The two-phase high precision bead data was used to compare the resulting estimates from k-means cluster analysis to results obtained from indicator kriging in the software package 3DMA. Interfacial area estimates were computed by voxel counting, 2-point correlation functions, marching cubes, and Blob3D. Four different marching cubes (Binary MC, Median MC, Gauss MC, and Resample MC) estimates were computed for comparison purposes, all of which, except Binary MC, consisted of filtering the segmented

data prior to constructing the isosurfaces in Amira™. Our method was also compared to Blob3D since it is a commonly used image processing software package. The capillary tube data served as a simple three-phase system for testing the reliability of the interfacial area estimates. Voxel counting, two-point correlation functions, and four different marching cubes estimates were compared using the three capillary tube data sets, all of which were segmented by k-means cluster analysis. PMMC [30] estimates were also included in the comparison as well as estimates obtained using the method of Culligan et al. [15, 16]. The effects of resolution on the resulting estimates were also investigated for both the high precision glass beads and the capillary tube data.

Void ratio profiles (as a function of depth) for the high precision beads showed that there was no observable difference between the estimates obtained from the two different segmentation routines and two different resolutions. Additionally, the volume averaged porosity estimates obtained from either segmentation routines was within 1.5% error of the laboratory porosity estimates. Interfacial area estimates showed that voxel counting and two-point correlation functions significantly overestimated (25–45%) the laboratory estimates, whereas all MC-based estimates, and Blob3D, were within 15%. The interfacial area estimates obtained from the higher resolution data exceeded the lower resolution estimates by a factor of 1.04–1.09 in all cases. Furthermore, all interfacial area estimates obtained from data segmented by indicator kriging were slightly lower than the corresponding estimates obtained from data segmented by k-means; however, the differences were minimal. Thus, it was shown that for the two-phase, high precision beads the resulting estimates were not sensitive to the two segmentation routines used here.

Inspection of the capillary tube data showed that voxel counting and 2-point correlation functions resulted in interfacial area estimates that were significantly higher than the analytical estimate, whereas the MC-based estimates, including PMMC and the Culligan method, were in good agreement with the analytical estimate. It was also shown that the MC methods generally underestimated the analytical estimate. The MC estimates with pixelation effects were closer to the analytical estimate than those that had been smoothed prior to constructing the isosurfaces, which suggests that smooth isosurfaces are not necessarily the best estimate when applying MC to CMT data. The interfacial area estimates obtained using Amira™ were also in agreement with those obtained using PMMC. This was somewhat surprising since the PMMC algorithm bypasses the segmentation step and provides a better representation of the fluid surfaces at the three-phase contact line. An increase in the resolution by a factor of 2 or 4 did not result in significant improvements in the interfacial area estimates; however, an increase by a factor of 8 led to significant overestimation mainly due to noise produced at this resolution. Further filtering of the gray-scale data could perhaps eliminate some of this noise, as could changes in the experimental procedure, for instance by using longer exposure times during tomographic data collection. As expected, the 13.0-, 6.5-, and 3.3-μm resolution results indicate that the interfacial area estimates are relatively consistent for this range of resolutions, suggesting that the estimates are not highly dependent on the image resolution. In any given data set, there should be a range of resolutions in which all of the important features are resolved in the images and thus, the interfacial area estimates should not change significantly. At sufficiently high resolutions, the images would resolve features, such as nanoscale roughness (see [26]), that would invalidate the chosen analytical model, in our case a spherical cap.

Overall, we have shown that the method presented here to obtain phase distributions and interfacial area estimates was in excellent agreement with measured values, as well as with other methods that are commonly used in the literature (i.e., indicator kriging via 3DMA, Blob3D, and PMMC). In addition, the improvements to the segmentation routine presented here were found to result in more consistent interfacial area estimates than the routine previously used by Culligan et al. [15, 16].

Acknowledgements Porter and Wildenschild were supported by NSF-EAR-06101108 and NSF-EAR-0337711. The authors would like to thank Marcel Schaap for his assistance with the 2-point correlation function data analysis. Additionally, we like to thank James McClure for the interfacial area estimates obtained from the porous media marching cubes algorithm. A portion of this work was conducted at GeoSoilEnviroCARS (Sector 13), Advanced Photon Source (APS), Argonne National Laboratory. GeoSoilEnviroCARS is supported by the National Science Foundation—Earth Sciences (EAR-0622171) and Department of Energy—Geosciences (DE-FG02-94ER14466). Use of the Advanced Photon Source was supported by the U. S. Department of Energy, Office of Science, Office of Basic Energy Sciences, under Contract No. DE-AC02-06CH11357. We thank all of the staff for research support.

References

1. Al-Raoush, R.I., Wilson, C.S.: Extraction of physically realistic pore network properties from three-dimensional synchrotron x-ray microtomography images of unconsolidated porous media systems. J. Hydrol. **300**, 44–64 (2005). doi:10.1016/j.jconhyd.2004.12.001

2. Al-Raoush, R.I., Wilson, C.S.: A pore-scale investigation of a multiphase porous media system. J. Cont. Hydrol. **77**, 67–89 (2005). doi:10.1016/j.jhydrol.2004.05.005
3. Altman, S.J., Peplinski, W.J., Rivers, M.L.: Evaluation of synchrotron x-ray computerized microtomography for the visualization of transport processes in low-porosity materials. J. Contam. Hydrol. **78**, 167–183 (2005). doi:10.1016/j/jconhyd.2005.05.004
4. Arns, C., Knackstedt, M., Mecke, K.: Reconstructing complex materials via effective grain shapes. Phys. Rev. Lett. **91**(21), 215506-1–215506-4 (2003)
5. Betson, M., Barker, J., Barnes, P., Atkinson, T.: Use of synchrotron tomographic techniques in the assessment of diffusion parameters for solute transport in groundwater flow. Transp. Porous Media **60**, 217–223 (2005). doi:10.1007/s11242-004-5737-0
6. Brusseau, M.L., Peng, S., Schnaar, G., Costanza-Robinson, M.S.: Relationship among air–water interfacial area, capillary pressure and water saturation for a sandy porous medium. Water Resour. Res. **42**, W03501 (2006). doi:10.1029/2005WR004058
7. Brusseau, M.L., Peng, S., Schnaar, G., Murao, A.: Measuring air–water interfacial areas with X-ray microtomography and interfacial partitioning tracer tests. Environ. Sci. Technol. **41**, 1956–1961 (2007)
8. Carlson, W.D.: Three-dimensional imaging of earth and planetary materials. Earth Planet. Sci. Lett. **249**, 133–147 (2006). doi:10.1016/j.epsl.2006.06.020
9. Chen, D., Pyrak-Nolte, L.J., Griffin, J., Giordano, N.J.: Measurement of interfacial are per volume for drainage and imbibition. Water Resour. Res. **43**, W12504 (2007). doi:10.1029/2007WR006021
10. Cheng, J.T., Pyrak-Nolte, L.J., Nolte, D.D., Giordano, N.J.: Linking pressure and saturation through interfacial areas in porous media. Geophys. Res. Lett. **31**, L08502 (2004)
11. Clausnitzer, V., Hopmans, J.W.: Determination of phase-volume fractions from tomographic measurements in two-phase systems. Adv. Water Resour. **22**(6), 577–584 (1999)
12. Clausnitzer, V., Hopmans, J.W.: Pore-scale measurements of solute breakthrough using microfocus x-ray computed tomography. Water Resour. Res. **36**(8), 2067–2079 (2000)
13. Coles, M.E., Hazlett, R.D., Spanne, P., Soll, W.E., Muegge, E.L., Jones, K.W.: Pore level imaging of fluid transport using synchrotron x-ray microtomography. J. Pet. Sci. Eng. **19**, 55–63 (1998)
14. Costanza-Robinson, M.S., Harrold, K.H., Lieb-Lappen, R.M.: X-ray microtomography determination of air–water interfacial area-water saturation relationships in sandy porous media. Environ. Sci. Technol. **42**, 2949–2956 (2008) (Accepted)
15. Culligan, K.A., Wildenschild, D., Christensen, B.S., Gray, W.G., Rivers, M.L.: Pore-scale characteristics of multiphase flow in porous media: a comparison of air–water and oil–water experiments. Adv. Water Resour. **29**, 227–238 (2006)
16. Culligan, K.A., Wildenschild, D., Christensen, B.S., Gray, W.G., Rivers, M.L., Tompson, A.B.: Interfacial area measurements for unsaturated flow through porous media. Water Resour. Res. **40**, W12413 (2004). doi:10.1029/2004WR003278
17. Dalla, E., Hilpert, M., Miller, C.T.: Computation of the interfacial area for two-fluid porous systems. J. Contam. Hydrol. **56**, 25–48 (2002)
18. Flin, F., Brzoska, J.B., Coeurjolly, D., Pieritz, R.A., Lesaffre, B., Coléou, C., Lamboley, P., Teytaud, O., Vignoles, G.L., Delesse, J.F.: Adaptive estimation of normals and surface area for discrete 3-D objects: application to snow binary data from X-ray tomography. IEEE Trans. Image Proc. **14**(5), 585–596 (2005)
19. Fredrich, J.T., DiGiovanni, A.A., Noble, D.R.: Predicting macroscopic transport properties using microscopic image data. J. Geophys. Res. **111**, B03201 (2006). doi:10.1029/2005JB003774
20. Gallagher, N.C., Wise, G.L.: A theoretical analysis of the properties of median filters. IEEE Trans. Acoust. Speech Signal Process. **29**(6), 1136–1141 (1981)
21. Gerig, G., Kubler, O., Kikinis, R., Jolesz, F.: Nonlinear anisotropic filtering of mri data. IEEE Trans. Med. Imag. **11**(2), 221–232 (1992)
22. Hopmans, J.W., Vogel, T., Koblik, P.D.: X-ray tomography of soil water distribution in one-step outflow experiments. Soil Sci. Soc. Am. J. **56**, 355–362 (1992)
23. Kaestner, A., Lehmann, E., Stampanoni, M.: Imaging and image processing in porous media research. Adv. Water Resour. **31**, 1174–1187 (2008). doi:10.1016/j.advwatres.2008.01.022
24. Ketcham, R.A.: BLOB3D User's Guide (2004). ftp://ctlab.geo.utexas.edu/Blob3D/
25. Ketcham, R.A., Iturrino, G.J.: Nondestructive high-resolution visualization and measurement of anisotropic effective porosity in complex lithologies using high-resolution x-ray computed tomography. J. Hydrol. **302**, 92–106 (2005). doi:10.1016/j.jhydrol.2004.06.037
26. Kim, H., Rao, P.S.C., Annable, M.D.: Consistency of the interfacial tracer technique: experimental evaluation. J. Contam. Hydrol. **40**, 79–94 (1999)
27. Lindquist, W.: 3DMA General Users Manual (1999). Stony Brook AMS Preprints. http://www.ams.sunysb.edu/papers/papers99.html
28. Lindquist, W., Venkatarangan, A.: Investigating 3d geometry of porous median from high resolution images. Phys. Chem. Earth (A) **25**(7), 593–599 (1999)
29. Lindquist, W.B., Lee, S.M., Coker, D.A., Jones, K.W., Spanne, P.: Medial axis analysis of void structure in three-dimensional tomographic images of porous media. J. Geophys. Res. **101**(B4), 8297–8310 (1996)
30. McClure, J., Adalsteinsson, D., Pan, C., Gray, W., Miller, C.: Approximation of interfacial properties in multiphase porous media systems. Adv. Water Resour. **30**(1), 354–365 (2007)
31. Montemagno, C.D., Ma, Y.: Measurement of interfacial surface areas for two-phase flow in porous media from pvi data. In: van Genuchten, M.T., Leije, F., Wu, L. (eds.) Characterization and Measurements of Hydraulic Properties of Unsaturated Porous Media, pp. 121–132. University of California Press, Riverside (1999)
32. Oh, W., Lindquist, B.: Image thresholding by indicator kriging. IEEE Trans. Pattern Anal. Mach. Intell. **21**(7), 590–602 (1999)
33. Øren, P., Bakke, S.: Reconstruction of berea sandstone and pore-scale modeling of wettability effects. J. Pet. Sci. Eng. **39**, 177–199 (2003). doi:10.1016/S0920-4105(03)00062-7
34. Pal, N.R.: On minimum cross-entropy thresholding. Pattern Recogn. **29**(4), 575–580 (1996)
35. Pappas, T.N.: An adaptive clustering algorithm for image segmentation. IEEE Trans. Signal Process. **40**(4), 901–914 (1992)
36. Patzek, T.W.: Verification of a complete pore network simulator of drainage and imbibition. SPE J. **6**, 144–156 (2001)
37. Perona, P., Malik, J.: Scale-space and edge detection using anisotropic diffusion. IEEE Trans. Pattern Anal. Mach. Intel. **12**(7), 629–639 (1990)
38. Petitot, J.: An introduction to the Mumford-Shah segmentation model. J. Physiol. Paris **97**, 335–342 (2003). doi:10.1016/j.jphysparis.2003.09.007
39. Prodonavić, M., Lindquist, W.B., Seright, R.: Porous structure and fluid partitioning in polyethylene cores from 3D

X-ray microtomography imaging. J. Colloid Interface Sci. **298**, 282–297 (2006). doi:10.1016/j.jcis.2005.11.053
40. Prodonavić, M., Lindquist, W.B., Seright, R.: 3d image-based characterization of fluid displacement in berea core. Adv. Water Resour. **30**, 214–226 (2007). doi:10.1016/j.advwatres.2005.05.015
41. Rivers, M.L.: GSECARS Tomography Processing Software (2001). http://cars9.uchicago.edu/software/idl/tomography.html
42. Schaap, M.G., Lebron, I.: Using microscope observations of thin sections to estimate soil permeability with the Kozeny–Carman equation. J. Contam. Hydrol. **251**, 186–201 (2001)
43. Scheckel, K.G., Hamon, R., Jassogne, L., Rivers, M., Lombi, E.: Synchrotron X-ray absorption-edge computed microtomography imaging of thallium compartmentalization in Iberis intermedia. Plant Soil **290**(1–2), 51–60 (2007). doi:10.1007/s11104-006-9102-7
44. Schnaar, G., Brusseau, M.L.: Pore-scale characterization of organic immiscible-liquid morphology in natural porous media using synchrotron X-ray microtomography. Environ. Sci. Technol. **39**, 8403–8410 (2005)
45. Schnaar, G., Brusseau, M.L.: Characterizing pore-scale configuration of organic immiscible liquid in multi-phase systems using synchrotron X-ray microtomography. Vadose Zone J. **5**, 641–648 (2006)
46. Sezgin, M., Sankur, B.: Selection of thresholding methods for non-destructive testing applications. In: Image Processing, 2001. Proceedings. 2001 International Conference on, vol. 3, pp. 764–767 (2001). doi:10.1109/ICIP.2001.958231
47. Sezgin, M., Sankur, B.: Survey over image thresholding techniques and quantitative performance evaluation. J. Electron. Imaging **13**(1), 146–165 (2004)
48. Sheppard, A.P., Sok, R.M., Averdunk, H.: Techniques for image enhancement and segmentation of tomographic images of porous materials. Phys. A **339**, 145–151 (2004). doi:10.1016/j.physa.2004.03.057
49. Silin, D., Patzek, T.: Pore space morphology analysis using maximal inscribed spheres. Phys. A **371**, 336–360 (2006). doi:10.1016/j.physa.2006.04.048
50. Song, S.R., Jones, K.W., Lindquist, W.B., Dowd, B.A., Sahagian, D.L.: Synchrotron X-ray computed microtomography studies of vesiculated basaltic rocks. Bull. Volcanol. **63**, 252–263 (2001)
51. Thieme, J., Schneider, G., Knöchel, C.: X-ray tomography of a microhabitat of bacteria and other soil colloids with sub-100 nm resolution. Micron **34**, 339–344 (2003). doi:10.1016/S0968-4328(03)000061-1
52. Torquato, S.: Random Heterogeneous Materials Microstructure and Microscopic Properties. Springer, New York (2002)
53. Turner, M., Knüfing, L., Arns, C., Sakellariou, A., Senden, T., Sheppard, A., Sok, R., Limaye, A., Pinczewski, W., Knackstedt, M.: Three-dimensional imaging of multiphase flow in porous media. Phys. A **339**, 166–172 (2004). doi:10.1016/j.physa.2004.03.059
54. Wildenschild, D., Hopmans, J.W., Rivers, M.L., Kent, A.J.: Quantitative analysis of flow processes in a sand using synchrotron-based X-ray microtomography. Vadose Zone J. **4**, 112–126 (2005)
55. Wildenschild, D., Hopmans, J.W., Vaz, C., Rivers, M.L., Rikard, D., Christensen, B.S.: Using X-ray computed microtomography in hydrology: systems, resolution and limitations. J. Hydrol. **267**, 285–297 (2002)